ACS NANO

Cite This: ACS Nano 2017, 11, 11127−11134

www.acsnano.org

ARTICLE

Fast Image-Guided Stratification Using Anti-Programmed Death Ligand 1 Gold Nanoparticles for Cancer Immunotherapy

Rinat Meir,[†,‡,∥] Katerina Shamalov,[§,∥] Tamar Sadan,[†,‡] Menachem Motiei,[†,‡] Gur Yaari,[†] Cyrille J. Cohen,[*,§] and Rachela Popovtzer[*,†,‡]

[†]Faculty of Engineering, [‡]The Institute of Nanotechnology and Advanced Materials, and [§]Laboratory of Tumor Immunology and Immunotherapy, Goodman Faculty of Life Sciences, Bar-Ilan University, Ramat Gan 52900, Israel

Supporting Information

ABSTRACT: **Cancer immunotherapy has made enormous progress in offering safer and more effective treatments for the disease. Specifically, programmed death ligand 1 antibody (αPDL1), designed to perform immune checkpoint blockade (ICB), is now considered a pillar in cancer immunotherapy. However, due to the complexity and heterogeneity of tumors, as well as the diversity in patient response, ICB therapy only has a 30% success rate, at most; moreover, the efficacy of ICB can be evaluated only two months after start of treatment. Therefore, early identification of potential responders and nonresponders to therapy, using noninvasive means, is crucial for improving treatment decisions. Here, we report a straightforward approach for fast, image-guided prediction of therapeutic response to ICB. In a colon cancer mouse model, we demonstrate that the combination of computed tomography imaging and gold nanoparticles conjugated to αPDL1 allowed prediction of therapeutic response, as early as 48 h after treatment. This was achieved by noninvasive measurement of nanoparticle accumulation levels within the tumors. Moreover, we show that the nanoparticles efficiently prevented tumor growth with only a fifth of the standard dosage of clinical care. This technology may be developed into a powerful tool for early and noninvasive patient stratification as responders or nonresponders.**

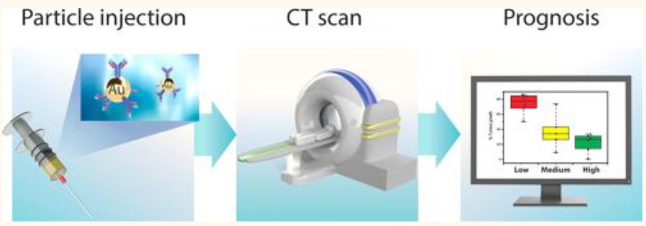

KEYWORDS: *gold nanoparticles, cancer immunotherapy, stratification, computed tomography, αPDL1, imaging*

Immune checkpoint blockade (ICB) is one of the main strategies in cancer immunotherapy and has greatly advanced cancer treatment.[1−4] In healthy tissue, immune checkpoints play an important role in maintaining immune homeostasis by downregulating cytotoxic T-cell activity. Yet in many types of cancer, immune checkpoints such as programmed death ligand 1 (PDL1) are overexpressed on tumor cells[5−9] and, thus, inhibit the antitumor immune response.[1−4] As many immune checkpoints are induced by receptor−ligand interaction, they can be blocked by antibodies. Several antibodies have been approved for ICB therapy in the clinic[5−9] and have shown highly promising results. However, ICB therapy has a limited success rate (of no more than 30%). The therapeutic success of ICB is affected by the complex interplay between the immune system, the tumor microenvironment, and multiple factors within the tumor.[10] Therefore, patient response is diverse and currently impossible to predict at the early stages of treatment. The earliest point for evaluating ICB efficacy in patients is only two months after commencing treatment. Furthermore, the amplified T-cell activation that ICB triggers can lead to a broad range of adverse and off-target effects.[11,12] Therefore, it is important to develop techniques to predict, at an early time point, whether ICB will produce the desired therapeutic response in an individual patient. This is especially pertinent in regard to patients with advanced cancer, as the number of therapeutic options becomes increasingly restricted with the progression of the disease.[13−18]

Cancer therapies have been greatly enhanced by the use of nanotechnology.[19−22] Nanoparticles are able to overcome biological barriers and achieve enhanced uptake in cancer cells, which has improved parameters such as the drug therapeutic index, *via* increase of drug efficacy and reduction of side effects.[14,22−25] Therefore, we surmised that a nanotherapy-based approach could potentially promote ICB treatments.

In the present study, we designed theranostic nanoparticles that integrate diagnostic and therapeutic functions into a single

Received: July 26, 2017
Accepted: October 13, 2017
Published: October 13, 2017

DOI: 10.1021/acsnano.7b05299
ACS Nano 2017, 11, 11127−11134

nanoparticle formulation. PDL1 antibody was conjugated to gold nanoparticles (αPDL1-GNPs) and examined in a mouse colon carcinoma model. Although the dosage of conjugated αPDL1 that was administered was equivalent to only one-fifth of the standard of care, it achieved a similar therapeutic effect and no toxicity was observed. In addition, the gold nanoparticle core served as a contrast agent for CT imaging[26−31] and enabled noninvasive, longitudinal tracking of the αPDL1-GNPs in vivo. As early as 48 h after treatment onset, CT imaging revealed intersubject variability in αPDL1-GNP tumor uptake, which significantly correlated with tumor growth inhibition. These findings enabled prompt stratification of subjects as responders or nonresponders. Thus, this fast and straightforward nanomedicine-based, image-guided stratification approach had a dual impact: lowering the effective dose and predicting therapeutic outcome based on tumor uptake. This approach could potentially be translated to humans, as depicted in Figure 1.

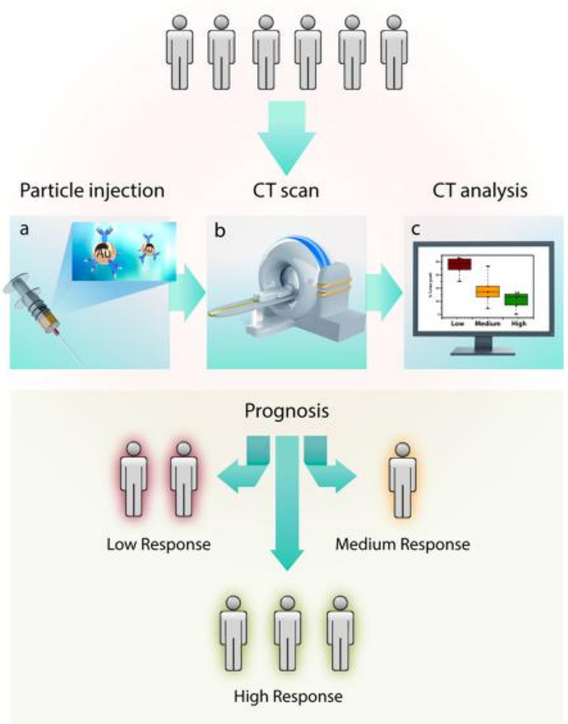

Figure 1. Nanomedicine predicts immune response *via* imaging. Proposed strategy: (a) gold nanoparticles are conjugated to anti-PDL1 and systemically injected; (b) 48 h post injection, subjects undergo a CT scan, and (c) analysis of signal intensity at the tumor enables stratifying subjects as high, medium, or low responders. Subjects indicated as high responders are expected to exhibit a long-lasting immune response following treatment, in the form of T-cell infiltration, which will inhibit tumor growth.

RESULTS

Theranostic Nanoparticles Engineered for Immunotherapy and CT Diagnostics. To obtain theranostic nanoparticles, 20 nm gold nanoparticle cores were synthesized and PEGylated and then conjugated to PDL1 antibody (αPDL1-GNPs). Control nanoparticles were designed by conjugation of IgG antibody to PEGylated gold nanoparticles (IgG-GNPs) with similar characteristics of size, charge and CT contrast. The fully detailed characteristics of the nanoparticles, including stability and biocompatibility assays, are included in the Supporting Information (Supplementary Figures 1−4).

Blocking Immune Checkpoint Ligand in Cancer Cells with Theranostic Nanoparticles. We first examined the function of αPDL1-GNPs as immune checkpoint blockers *in vitro*, in murine B16 melanoma and MC38 colon carcinoma cell lines. The cell lines were incubated with αPDL1-GNPs or the control IgG-GNPs, and expression levels of PDL1 were measured by FACS. Nontreated and IgG-treated B16 and MC38 cells showed high expression of PDL1 (91.5% and 86.6% of total cells, respectively), while cells treated with αPDL1-GNPs showed dramatically reduced PDL1 expression (17.1% and 23.9%, respectively) (Figure 2a). These results indicate that αPDL1-GNPs bind to the immune checkpoint ligand on the cancer cell surface, and suggest that this approach may facilitate T cell activation *in vivo*.

Next, we examined whether αPDL1-GNPs can actively target PDL1 *in vivo*. Either αPDL1-GNPs or IgG-GNPs, as control, were intravenously injected into tumor-bearing C57BL/6 mice. After 48 h post injection, tumors were CT scanned and then dissected and collected for quantification of Au content using atomic absorption spectroscopy. The results demonstrated a higher amount of Au content in tumors of mice treated with αPDL1-GNPs as compared with control IgG-GNPs (70% higher tumor uptake, Figure 2b). Biodistribution data can be found in the Supporting Information (Figure 5). CT images (Figure 2c,d) demonstrated that the αPDL1-GNPs were able to accumulate and penetrate within the tumor tissue, while IgG-GNPs demonstrate low uptake in the tumor. These results indicate that conjugation of PDL1 antibody to GNPs enhances tumor uptake.

Enhancing Therapeutic Efficacy of PDL1 Antibody with Theranostic Nanoparticles. We next tested the therapeutic efficacy of αPDL1-GNPs in a mouse model for colon carcinoma. C57BL/6 mice were inoculated with MC38 cells and 1 week later received an IV injection of either αPDL1-GNPs, IgG-GNPs, soluble PDL1 antibody (at a dose equivalent to that of antibody conjugated to particles; termed “low-αPDL1”), soluble PDL1 antibody (standard of care dose, 5 times the equivalent dose; termed “high-αPDL1”), or saline (n = 7 for each group). Tumor growth was measured over time. We found that both αPDL1-GNPs and high-αPDL1 significantly inhibited tumor growth rate, as compared with all other control groups ($p < 0.039$ and $p < 0.043$ respectively; Figure 3a). Yet although αPDL1-GNPs and high-αPDL1 show similar therapeutic efficacy, the nanoparticle-based treatment achieved the same therapeutic impact, with only a fifth of standard dose of care. No negative effect of treatment was seen on mouse weight during the experimental period (Supplementary Figure 6).

At the conclusion of the experiment (day 11), tumors were removed, and tumor-infiltrating lymphocytes (TILs) were quantified and measured by FACS. The number of TILs within tumors of the αPDL1-GNPs and free αPDL1 treatment groups was higher than the number of TILs found for the control groups (saline and IgG-GNPs; $p < 0.022$ *versus* saline-treated group). This indicates that αPDL1-GNPs mediate T cell infiltration similar to PDL1 antibody.

CT Demonstrates Time-Dependent Tumor Accumulation and Penetration of Theranostic Nanoparticles. We next longitudinally tracked αPDL1-GNPs *in vivo* using noninvasive CT imaging in a colon carcinoma mouse model.

DOI: 10.1021/acsnano.7b05299
ACS Nano 2017, 11, 11127−11134

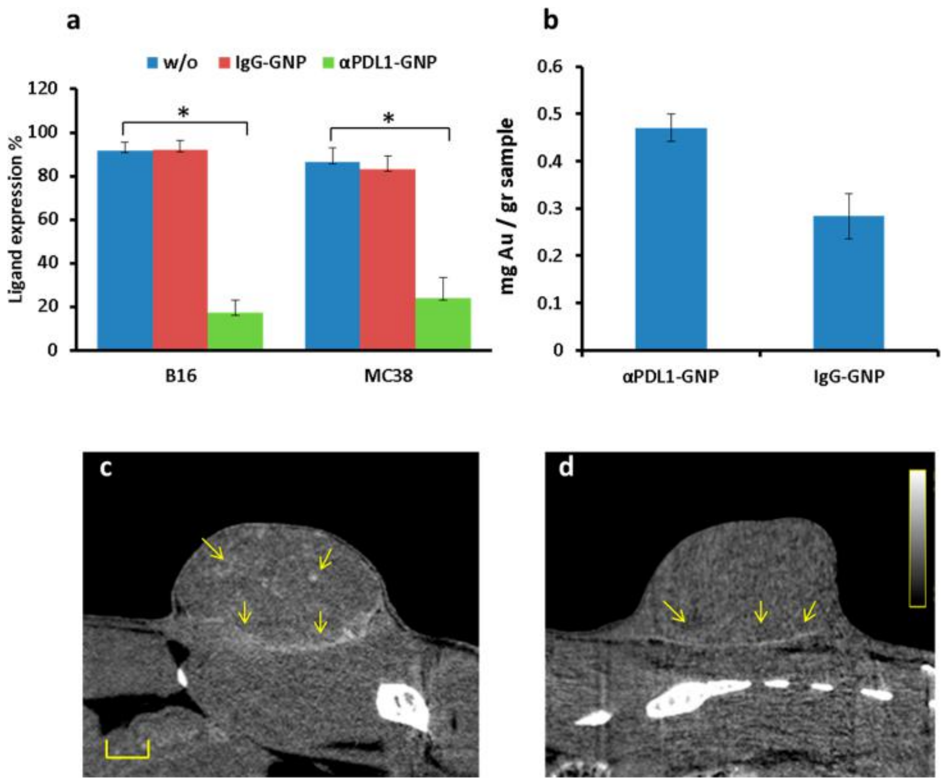

Figure 2. αPDL1-GNPs block PDL1 on cancer cells *in vitro* and actively target the tumor in vivo. (a) B16 and MC-38 cells were incubated with αPDL1-GNPs (1 h). Free ligand expression was assessed by flow cytometry staining of mouse PDL1. Nontreated cells ("w/o particles") or cells treated with IgG-GNPs were used as negative controls. αPDL1-GNP-treated cells showed significantly lower ligand expression compared with IgG-GNP treated cells (*$p < 0.05$; Student's paired *t* test). Results presented as mean $\pm$ SEM (b−d) αPDL1-GNPs and control IgG-GNPs were IV injected to tumor bearing C57BL/6 mice; 48 h later, tumors were imaged by CT and then collected for analytical measurement of Au. (b) Higher gold accumulation within the tumor was found for αPDL1-GNP treated mice as compared with IgG-GNP treated mice. CT images show accumulation of the two nanoparticle types in the tumor; however, (c) αPDL1-GNPs penetrate the tumor with high tumor uptake, while (d) IgG-GNPs demonstrate low tumor uptake. Scale bar is 1 mm.

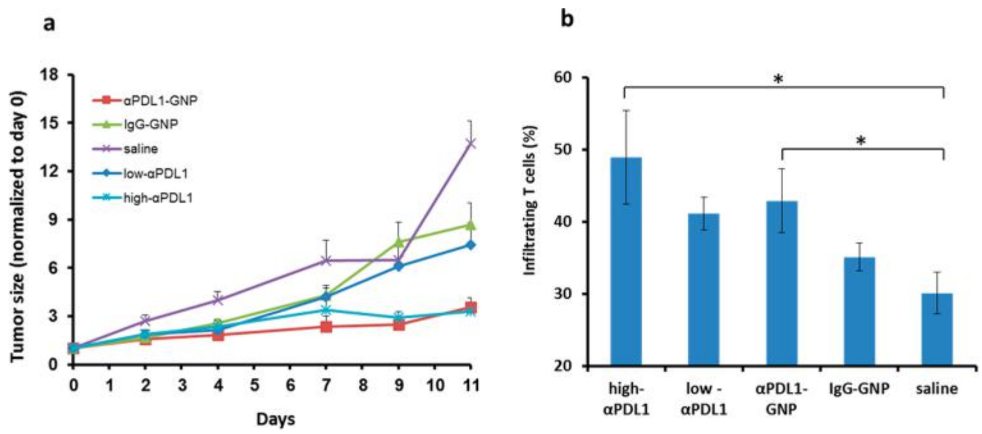

Figure 3. Theranostic nanoparticles enhance the therapeutic efficacy of PDL1 antibody and mediate T cell infiltration into tumors. Mice were treated with either αPDL1-GNPs, IgG-GNPs, free-αPDL1 (low or high dose), or saline only. (a) Comparison of tumor growth rate in mice. (b) Comparison of tumor infiltrating lymphocytes (TILs) in tumor tissue. Results are presented as mean $\pm$ SEM (*$p < 0.05$; Student's paired *t* test).

C57BL/6 mice were inoculated with MC38 cells, and 1 week later, tumor-bearing mice were administered αPDL1-GNPs. CT imaging was conducted every 24 h, over week post-treatment. Tumor accumulation of αPDL1-GNPs was calculated based on the number of gold voxels per tumor area. The large number of high density voxels in the tumor allowed imaging of the tumor, as seen in a full body image (Figure 4). We found that the maximum accumulation of nanoparticles within the tumor was achieved 48 h post injection (Figure 4). Intriguingly, αPDL1-GNPs did not only accumulate at the periphery but showed intratumoral penetration. It is notable that the 2D slice image of the center of the tumor (Figure 5, middle) also clearly shows intratumoral penetration of the particles.

DOI: 10.1021/acsnano.7b05299
ACS Nano 2017, 11, 11127−11134

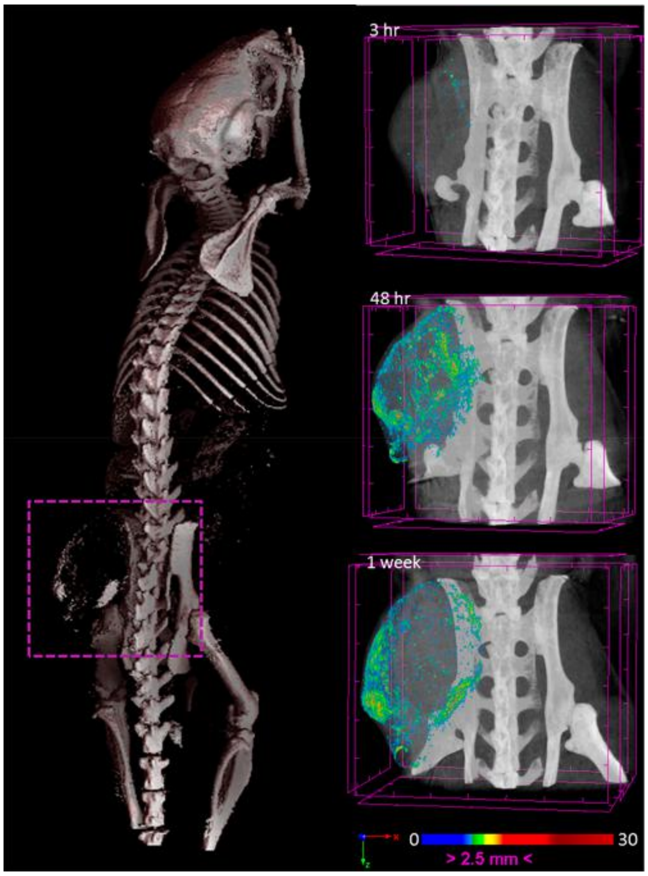

Figure 4. CT images demonstrating nanoparticle accumulation at the tumor. 3D volume rendered image of mouse administered with αPDL1-GNPs. Left figure: Demarcation of tumor location on the back of the mouse. Intensity in the tumor area is in the range of bone intensity. Right figures, top to bottom: Time-dependent accumulation of particles: top, 3 h post injection; mid, 48 h post injection; bottom, 1 week post injection. Maximum uptake was observed at 48 h. Colors indicating high density of particles are shown within the tumor area.

CT Reveals Large Variations in Tumor Uptake. Close examination of the CT signal quantification data revealed a considerable variation between mice, with some showing higher levels, and others lower levels, of tumor uptake of αPDL1-GNPs. This variation is also demonstrated in representative 3D and 2D CT volume rendering images of mice with high, medium, or low NP uptake (Figure 5).

We were intrigued by this finding and therefore conducted an additional experiment to further investigate a possible association between the degree of tumor uptake, at an early time point, and individual response to αPDL1-GNPs.

Predicting Response to Immunotherapy with Theranostic Nanoparticles. To determine whether such a correlation exists, mice (n = 20) were inoculated with MC38 cells and administered with the theranostic αPDL1-GNPs. Forty-eight hours after injection, the mice underwent a CT scan. Tumor growth was measured over 8 days after injection to evaluate response to therapy.

Our findings showed distinct patterns of response in mice. First, a linear correlation was found between the quantitative CT signal at 48 h and tumor growth at day eight (R^2 = 0.6162, Figure 6a). This result indicates that by using noninvasive CT imaging, early response, and tumor growth inhibition can be predicted at 48 h post injection. Moreover, plotting of the percentage of tumor growth in animals with low and high CT signal shows a small standard error, indicating that the therapeutic response can be accurately predicted (Figure 6b). However, in animals with intermediate CT signal, a large standard error was observed, indicating the inability to predict therapeutic response in the intermediate CT signal group. It is important to note that no correlation was observed with the control nanoparticles, and no correlation between tumor volume before treatment and CT uptake was found (Supplementary Figures 7 and 8).

As T-cells must directly contact cancer cells in order to kill them, we hypothesize that a correlation exists between T cell accumulation, at 48 h post treatment, and treatment outcome at a later time point. In order to investigate this, tumors were removed on day 8, and T cell infiltration was quantified and measured by FACS. We found that the degree of tumor growth correlated with T cell infiltration into the tumor tissue (Figure 6c). In addition, the CT signal correlated with T cell infiltration as well (Figure 6d). These results indicate a triangular correlation between the three parameters, namely, tumor growth, CT signal at 48 h, and T cell infiltration measured at the end of the experiment.

DISCUSSION

In the present study, we demonstrated the ability to noninvasively identify, at an early time point, potential responders and nonresponders to αPDL1-GNP therapy. The analysis of CT signal intensity at the tumor enabled stratifying subjects as high, medium, or low responders. High responders showed higher T-cell infiltration into tumor tissue.

Our theranostic nanoparticles are administered systemically, as are most therapeutic nanoparticles for solid tumor treatment. The particles can accumulate in the tumor *via* two modes—passively, through the enhanced permeability and retention (EPR) effect,[24,32−34] and actively, by targeting PDL1, which is highly expressed on the tumor cells. Multiple biological events that occur following systemic delivery of NPs can affect tumor uptake, including NP−protein interaction, blood circulation, interaction with the perivascular tumor microenvironment, tumor tissue penetration, and tumor cell internalization.[14,24] These different parameters render the overall particle uptake into a “black box” in individual patients and are difficult—even nearly impossible—to analyze.

The complexity and the heterogeneity of tumors emphasize the need for careful patient selection, to identify those most likely to benefit from a given therapy. Here we present a simple and straightforward method for providing the clinician with a prognostic indication regarding the initial response to the theranostic αPDL1-GNPs. This approach is fast and non-invasive, as it is performed using CT imaging, and does not require further extensive investigations of the “black box”.

Integrating diagnostic and therapeutic functions into a single NP formulation offers a strategy for monitoring the biodistribution, pharmacokinetics, and tumor accumulation of therapeutics and the progression of disease.[35−37] We show that this strategy can provide important insights into heterogeneities both within tumors and between subjects, for potential personalized treatment. However, other recent studies have suggested the use of companion imaging nanoparticles, rather than theranostic particles; this approach enables administration of imaging particles without a conjugated therapeutic agent, and does not require modification of the therapeutic particle.[13,15]

DOI: 10.1021/acsnano.7b05299
ACS Nano 2017, 11, 11127−11134

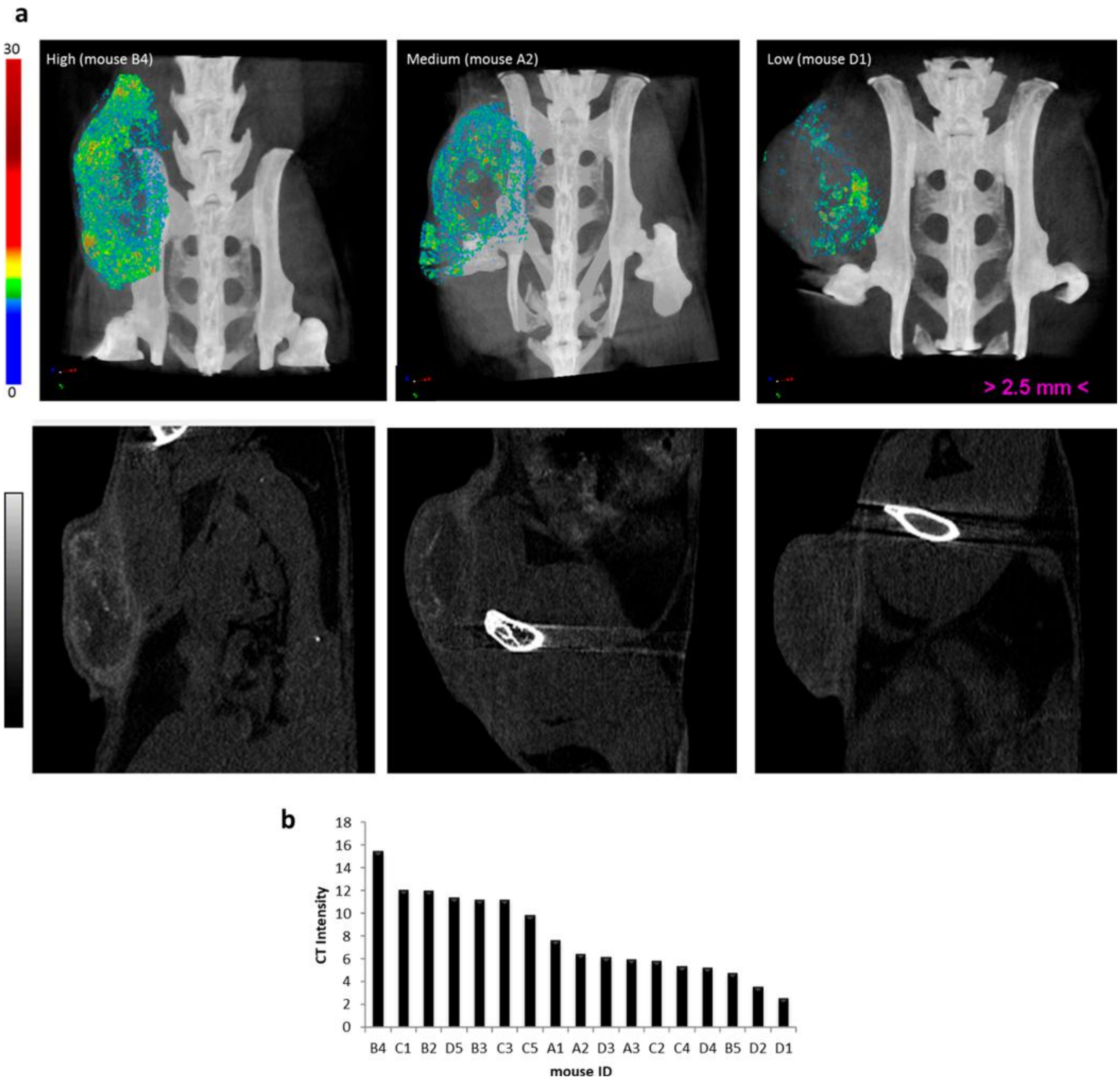

Figure 5. CT signal demonstrates large variations in tumor uptake. (a) Representative 3D (top panels) and 2D (bottom panels) CT images of mice with low, medium, or high CT signals. (b) Variability in αPDL1-GNP accumulation in 17 mice.

Yet the advantage of theranostic particles, as used here, is their reliability, accuracy, and precision in tracking the therapeutic agent. These features are crucial for immunotherapy, in which the "black box" consists of both the tumor and the adaptive immune system of an individual subject.

In regard to their therapeutic value, αPDL1-GNPs showed improved efficacy compared with the equivalent (low) dose of free PDL1 antibody. The effect of αPDL1-GNPs was similar to the effect of the standard αPDL1 dosage given in clinical care, even though only a fifth of this dosage was needed with the nanoparticles. Thus, the amount of immunotherapy drug can be greatly reduced using a more targeted strategy provided by the theranostic nanoparticles. This factor is crucial because severe side effects have been seen in clinical trials using the free antibody. As conjugating the antibody to the particles reduces the required dose, it will likely reduce the adverse effects as well, though this needs to be examined in future studies. Compared to the free drug, the GNP-conjugated drug may also show higher rates of tumor arrival and longer duration of tumor retention.

In summary, we present a straightforward strategy, based on immune nanoparticles and noninvasive imaging, which holds a combined prognostic and theranostic value. Our theranostic-nanoparticle CT imaging technology allows early prediction of response, and enhances ICB therapy. Subjects indicated as high responders exhibit a long-lasting immune response following treatment, likely due to higher T-cell infiltration, which inhibits tumor growth. The proposed concept could be applied to other immunotherapy antibodies and thereby expedite patient stratification and personalized nanomedicine.

DOI: 10.1021/acsnano.7b05299
ACS Nano 2017, 11, 11127−11134

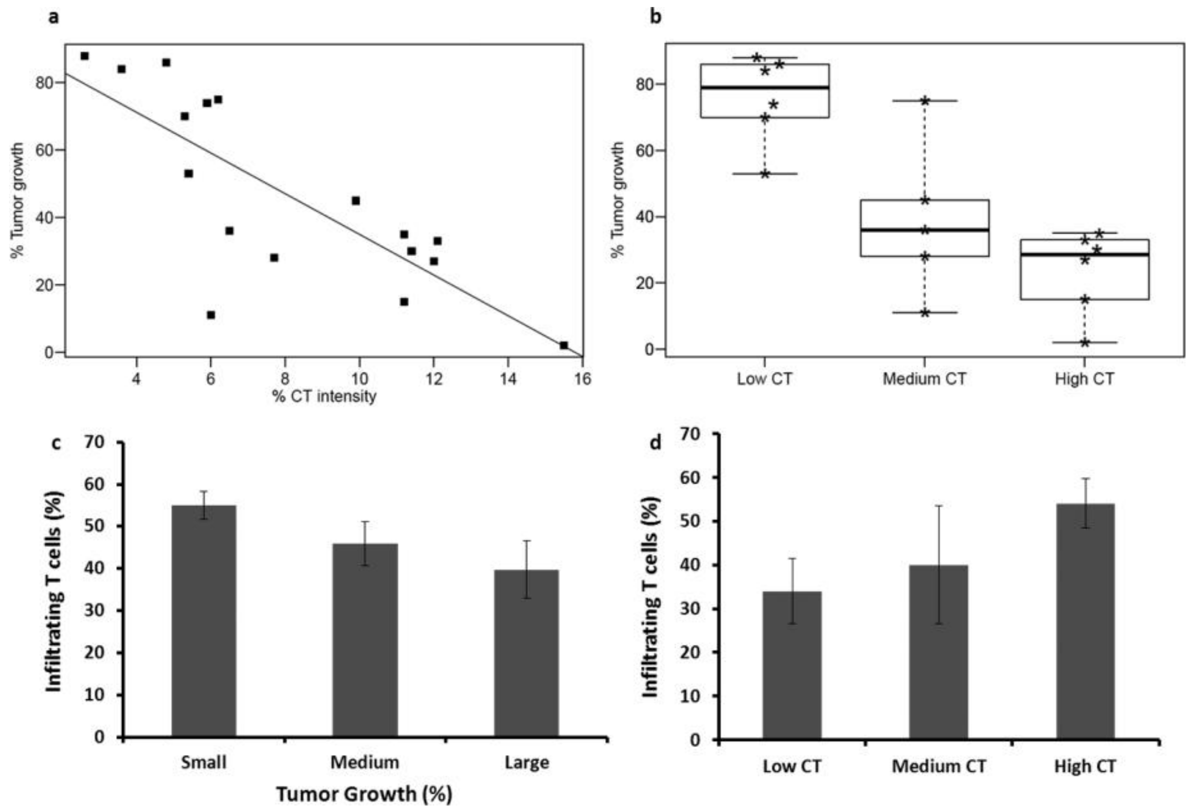

Figure 6. CT signal enables prediction of response to therapy. The tumor growth rate was measured 7 days post injection and was correlated to the signal intensity at 48 h. (a) Plotted correlation between signal intensity and tumor growth. Multiple *R*-squared: 0.6162. Adjusted *R*-squared: 0.5906. F-statistic: 24.08 with 15 DF. *p*-value: 0.0001897. (b) Subjects were divided into three groups according to the signal (low, medium, and high). Box plot shows that the CT signal intensity was able to predict response to the therapy. TIL infiltration correlates with tumor growth as well as with CT signal intensity. (c) T cell infiltration (8 days post injection) correlates with the change in tumor volume growth (%) 1 week post injection. The smaller the degree of tumor growth (%), the higher the percentage of TILs within tumor tissue. (d) T cell infiltration (8 days post injection) correlates with the CT signal at 48 h.

METHODS

GNP Synthesis, Conjugation and Characterization. *Synthesis.* Synthesis of 20 nm spherical GNPs was carried out using sodium citrate as a reducing agent, based on Enüstün and Turkevic's methodology.[38] A 414 μL portion of 50% w/V HAuCl4 solution was added to 200 mL of purified water, and the solution was heated in an oil bath on a heating plate until boiling. Then 4.04 mL of 10% sodium citrate solution were added, and the solution was stirred for 10 min. After being cooled to room temperature, the solution was centrifuged until precipitation of the nanoparticles.

Conjugation. GNPs were coated with a PEG layer. The PEG layer consists of a mixture of thiol-polyethylene-glycol (mPEG-SH) (~85%, MW ≈ 5 kDa) and a heterofunctional thiolPEG-acid (SH-PEG-COOH) (~15%, MW ≈ 5 kDa).[20,39−41] The PEG mixture was added in excess to the nanoparticles and the solutions were stirred for 4 h at room temperature. Following this step, the solutions were centrifuged in order to remove excess PEG molecules and reach higher concentrations. The PDL1 antibody layer (anti-PDL1, clone 10F.9G2, BioXcell, West Lebanon, NH) was then covalently conjugated to the carboxylic group of the SH-PEG-COOH, after activation with EDC (1-ethyl- 3-(3-(dimethylamino)propyl) carbodiimide HCl, Thermo Scientific) and NHS (*N*-hydroxysulfosuccinimide sodium salt, ChemImpex International) by adding all three to the PEG-GNP solution and stirring the mixture overnight. Centrifugation was performed until a final Au concentration of 30 mg mL^{-1} was reached.

Characterization. The size and charge of the GNPs was measured using dynamic light scattering (DLS) (NANO-flex, Particle matrix, Germany) and charge analysis (Rapid particle charge titrations, Stabino, Particle Matrix, Germany), as well as UV−vis spectroscopy (UV−vis; UV-1650 PC; Shimadzu Corp., Kyoto, Japan) The amount of conjugated antibody was determined by the Bradford protein assay. We then could further calculate the coupling ratio between the antibody and the particle which was determined to be 4 (protein/particle) ((1.42 mg (9.486e−9 mol) antibody was found to be conjugated to 2.4885e−9 mol GNPs)). Transmission electron microscopy (TEM) was used to demonstrate the coating of the GNPs. Uranyl acetate was used for negative staining and contrast images were acquired using a JEOL JEM-2010F FEG-TEM (JEOL, Japan) operated at 200 kV, equipped with a 2K × 2K Ultrascan CCD camera (Gatan, Inc., Warrendale, PA).

Cell Lines. Murine PDL1 positive cell line, MC-38 and B16 were cultured in DMEM (Biological Industries, Beth Haemek, Israel) supplemented with 10% heat-inactivated Fetal Bovine Serum (Biological Industries, Beth Haemek, Israel) and were maintained in a 37 °C and 5% CO_2 incubator.

FACS Analysis and Antibodies. Antimurine PDL1 was purchased from BioXCell and Fluorophore-labeled CD3ε from BioLegend (San Diego, CA).[42−44] Immunofluorescence, analyzed as the relative log fluorescence of live cells, was measured using a CyAn-ADP flow cytometer (Beckman Coulter, Brea). Approximately 1×10^5 cells were analyzed. Cells were stained in a FACS buffer made of PBS, 0.5% BSA, and 0.02% sodium azide.

Cell Cycle Assay. MC-38 cells were labeled with the gold nanoparticles (aPDL1-GNP, 30 mg/mL) for 1 h, washed with PBS, and transferred to the cells media for another 48 h. Next, cells were labeled with 1 μM propidium iodide (PI) (Sigma-Aldrich, Israel) and analyzed by flow-cytometry.

Animal Model and *in Vivo* Experiments. Two $\times 10^6$ cells were injected subcutaneously into the back flank area of C57BL/6 mice

DOI: 10.1021/acsnano.7b05299
ACS Nano 2017, 11, 11127−11134

aged 6 weeks (Harlan, Jerusalem, Israel). One week later, mice were received IV injection of the different particles, at a volume of 200 μL and a gold concentration of 30 mg/mL. αPDL1-GNPs, IgG-GNPs, saline and the "low-αPDL1" (73 μg of soluble PDL1 antibody) groups were administrated twice (once a week), while "high-αPDL1" group (200 μg of soluble PDL1 antibody) was administrated four times (twice a week). Tumor size was measured (every 2 days) in a blinded fashion using a caliper and calculated using the following formula: $[D \times d^2] \times \Pi/6$, where D is the largest tumor diameter and d its perpendicular one. In addition, tumor growth was measured by a 3D analysis by CT analyzer software. The study was conducted in compliance with the protocols approved by the Animal Care and Use Committees of Bar Ilan University, Ramat Gan, Israel.

FAAS Analysis. Flame atomic absorption spectroscopy (FAAS, SpectrAA 140, Agilent Technologies) was used to determine amounts of gold in the investigated samples. Cell samples from the *in vitro* experiments were dissolved in 100 μL of aqua regia acid (a mixture of nitric acid and hydrochloric acid in a volume ratio of 1:3) and diluted with purified water to a total volume of 4 mL. Tissues taken in the *in vivo* experiment were melted with 1 mL aqua regia acid and then evaporated and diluted to a total volume of 10 mL. After filtration of the samples, gold concentrations were determined according to absorbance values, with correlation with calibration curves, constructed from solution with known gold concentrations.

Mouse Tumor Digestion and T Cell Assessment. Tumors were removed and mince into small fragments. Cultures were then transferred into a HBSS media (Biological Industries, Beth Haemek, Israel) included with enzyme mix of Collagenase and DNase (Sigma-Aldrich) and incubate at rt for 1−3 h. Finally, cells were passed through 70 μm filter unit, washed in HBSS, and resuspended with an appropriate volume of plating media. T cell expression was assessed using flow cytometry by staining the single cell suspension (SCS) population with mouse-CD3ε chain antibody

Micro-CT Scans. *In vivo* scans of the tumor regions were performed using a micro-CT scanner (Skyscan High Resolution Model 1176) with a nominal resolution of 35 μm,[45,46] a 0.2 mm aluminum filter, and a tube voltage of 45 kV. Reconstruction was done with a modified Feldkamp41 algorithm using the SkyScanNRecon software accelerated by GPU.42. Ring artifact reduction, Gaussian smoothing (3%), and beam hardening correction (20%) were applied. Volume rendered three-dimensional (3D) images were generated using an RGBA transfer function in SkyScan CT-Volume ("CTVol") software.

Statistical Analysis. Statistical analyses were performed using a paired Student's t test. P values are one-tailed with testing level thresholds of α = 0.05 and indicated in the figures. Pearson's r coefficients were calculated to determine correlation.

ASSOCIATED CONTENT

Supporting Information

The Supporting Information is available free of charge on the ACS Publications website at DOI: 10.1021/acsnano.7b05299.

> Synthesis and characterization of αPDL1-GNPs and control IgG-GNPs; TEM images of the nanoparticles; stability of αPDL1-GNPs in PBS and serum; biocompatibility of αPDL1-GNPs demonstrated by cell-cycle analysis; biodistribution of the nanoparticles; changes in body weight of MC38 tumor-bearing mice; CT intensity does not correlate with tumor size; CT intensity does not correlate with tumor growth in control mice (PDF)

AUTHOR INFORMATION

Corresponding Authors

*E-mail: cyrille.cohen@biu.ac.il (Cancer Immunotherapy).
*E-mail: rachela.popovtzer@biu.ac.il (Nanomedicine).

ORCID

Rinat Meir: 0000-0001-6615-0288

Author Contributions

‖R.M. and K.S. contributed equally.

Notes

The authors declare no competing financial interest.

ACKNOWLEDGMENTS

We thank the Ministry of Science, Technology and Space for R.M.'s doctoral scholarship. We thank Merkel Technologies for conducting the Particle Matrix experiments and Michal Marcus for conducting the Bradford assay.

REFERENCES

(1) Mahmoudi, M.; Farokhzad, O. C. Cancer Immunotherapy: Wound-Bound Checkpoint Blockade. *Nat. Biomed. Eng.* **2017**, *1*, 31.

(2) Pardoll, D. M. The Blockade of Immune Checkpoints in Cancer Immunotherapy. *Nat. Rev. Cancer* **2012**, *12*, 252−264.

(3) Gettinger, S.; Herbst, R. S. B7-H1/PD-1 Blockade Therapy in Non-Small Cell Lung Cancer: Current Status and Future Direction. *Cancer J.* **2014**, *20*, 281−289.

(4) Philips, G. K.; Atkins, M. Therapeutic Uses of Anti-PD-1 and Anti-PD-L1 Antibodies. *Int. Immunol.* **2015**, *27*, 39−46.

(5) Boutros, C.; Tarhini, A.; Routier, E.; Lambotte, O.; Ladurie, F. L.; Carbonnel, F.; Izzeddine, H.; Marabelle, A.; Champiat, S.; Berdelou, A.; Lanoy, E.; Texier, M.; Libenciuc, C.; Eggermont, A. M. M.; Soria, J.-C.; Mateus, C.; Robert, C. Safety Profiles of Anti-CTLA-4 and Anti-PD-1 Antibodies Alone and in Combination. *Nat. Rev. Clin. Oncol.* **2016**, *13*, 473−486.

(6) Graziani, G.; Tentori, L.; Navarra, P. Ipilimumab: A Novel Immunostimulatory Monoclonal Antibody for the Treatment of Cancer. *Pharmacol. Res.* **2012**, *65*, 9−22.

(7) Guo, L.; Zhang, H.; Chen, B. Nivolumab as Programmed Death-1 (PD-1) Inhibitor for Targeted Immunotherapy in Tumor. *J. Cancer* **2017**, *8*, 410−416.

(8) Force, J.; Salama, A. First-Line Treatment of Metastatic Melanoma: Role of Nivolumab. *ImmunoTargets Ther.* **2017**, *6*, 1−10.

(9) Bilgin, B.; Sendur, M. A. N.; Bülent Akıncı, M.; Şener Dede, D.; Yalçın, B. Targeting the PD-1 Pathway: A New Hope for Gastrointestinal Cancers. *Curr. Med. Res. Opin.* **2017**, *33*, 749−759.

(10) Nishino, M.; Ramaiya, N. H.; Hatabu, H.; Hodi, F. S. Monitoring Immune-Checkpoint Blockade: Response Evaluation and Biomarker Development. *Nat. Rev. Clin. Oncol.* **2017**, DOI: 10.1038/nrclinonc.2017.88.

(11) Blasig, H.; Bender, C.; Hassel, J. C.; Eigentler, T. K.; Sachse, M. M.; Hiernickel, J.; Koop, A.; Satzger, I.; Gutzmer, R. Reinduction of PD1-Inhibitor Therapy. *Melanoma Res.* **2017**, *27*, 321.

(12) Wang, W.; Lie, P.; Guo, M.; He, J. Risk of Hepatotoxicity in Cancer Patients Treated with Immune Checkpoint Inhibitors: A Systematic Review and Meta-Analysis of Published Data. *Int. J. Cancer* **2017**, *141*, 1018−1028.

(13) Miller, M. A.; Gadde, S.; Pfirschke, C.; Engblom, C.; Sprachman, M. M.; Kohler, R. H.; Yang, K. S.; Laughney, A. M.; Wojtkiewicz, G.; Kamaly, N.; Bhonagiri, S.; Pittet, M. J.; Farokhzad, O. C.; Weissleder, R. Predicting Therapeutic Nanomedicine Efficacy Using a Companion Magnetic Resonance Imaging Nanoparticle. *Sci. Transl. Med.* **2015**, *7*, 314ra183.

(14) Shi, J.; Kantoff, P. W.; Wooster, R.; Farokhzad, O. C. Cancer Nanomedicine: Progress, Challenges and Opportunities. *Nat. Rev. Cancer* **2016**, *17*, 20.

(15) Pérez-Medina, C.; Abdel-Atti, D.; Tang, J.; Zhao, Y.; Fayad, Z. A.; Lewis, J. S.; Mulder, W. J.; Reiner, T. Nanoreporter PET Predicts the Efficacy of Anti-Cancer Nanotherapy. *Nat. Commun.* **2016**, *7*, 11838.

(16) Kulkarni, A.; Rao, P.; Natarajan, S.; Goldman, A.; Sabbisetti, V. S.; Khater, Y.; Korimerla, N.; Chandrasekar, V.; Mashelkar, R. A.; Sengupta, S. Reporter Nanoparticle That Monitors Its Anticancer

DOI: 10.1021/acsnano.7b05299
ACS Nano 2017, 11, 11127−11134

Efficacy in Real Time. *Proc. Natl. Acad. Sci. U. S. A.* **2016**, *113*, No. E2104.
(17) Roh, W.; Chen, P.-L.; Reuben, A.; Spencer, C. N.; Prieto, P. A.; Miller, J. P.; Gopalakrishnan, V.; Wang, F.; Cooper, Z. A.; Reddy, S. M.; Gumbs, C.; Little, L.; Chang, Q.; Chen, W.-S.; Wani, K.; De Macedo, M. P.; Chen, E.; Austin-Breneman, J. L.; Jiang, H. Integrated Molecular Analysis of Tumor Biopsies on Sequential CTLA-4 and PD-1 Blockade Reveals Markers of Response and Resistance. *Sci. Transl. Med.* **2017**, *9*, eaah3560.
(18) Weissleder, R.; Schwaiger, M. C.; Gambhir, S. S.; Hricak, H. Imaging Approaches to Optimize Molecular Therapies. *Sci. Transl. Med.* **2016**, *8*, 355ps16−355ps16.
(19) Popovtzer, A.; Mizachi, A.; Motiei, M.; Bragilovski, D.; Lubimov, L.; Levi, M.; Hilly, O.; Ben-Aharon, I.; Popovtzer, R. Actively Targeted Gold Nanoparticles as Novel Radiosensitizer Agents: An in Vivo Head and Neck Cancer Model. *Nanoscale* **2016**, *8*, 2678−2685.
(20) Dreifuss, T.; Betzer, O.; Shilo, M.; Popovtzer, A.; Motiei, M.; Popovtzer, R. A Challenge for Theranostics: Is the Optimal Particle for Therapy Also Optimal for Diagnostics? *Nanoscale* **2015**, *7*, 15175−15184.
(21) Ankri, R.; Ashkenazy, A.; Milstein, Y.; Brami, Y.; Olshinka, A.; Goldenberg-Cohen, N.; Popovtzer, A.; Fixler, D.; Hirshberg, A. Gold Nanorods Based Air Scanning Electron Microscopy and Diffusion Reflection Imaging for Mapping Tumor Margins in Squamous Cell Carcinoma. *ACS Nano* **2016**, *10*, 2349−2356.
(22) Brown, S. D.; Nativo, P.; Smith, J. A.; Stirling, D.; Edwards, P. R.; Venugopal, B.; Flint, D. J.; Plumb, J. A.; Graham, D.; Wheate, N. J. Gold Nanoparticles for the Improved Anticancer Drug Delivery of the Active Component of Oxaliplatin. *J. Am. Chem. Soc.* **2010**, *132*, 4678−4684.
(23) Qian, Y.; Qiu, M.; Wu, Q.; Tian, Y.; Zhang, Y.; Gu, N.; Li, S.; Xu, L.; Yin, R. Enhanced Cytotoxic Activity of Cetuximab in EGFR-Positive Lung Cancer by Conjugating with Gold Nanoparticles. *Sci. Rep.* **2015**, *4*, 7490.
(24) Bertrand, N.; Wu, J.; Xu, X.; Kamaly, N.; Farokhzad, O. C. Cancer Nanotechnology: The Impact of Passive and Active Targeting in the Era of Modern Cancer Biology. *Adv. Drug Delivery Rev.* **2014**, *66*, 2−25.
(25) Almeida, J. P. M.; Figueroa, E. R.; Drezek, R. A. Gold Nanoparticle Mediated Cancer Immunotherapy. *Nanomedicine* **2014**, *10*, 503−514.
(26) Kim, D.; Park, S.; Lee, J. H.; Jeong, Y. Y.; Jon, S. Antibiofouling Polymer-Coated Gold Nanoparticles as a Contrast Agent for in Vivo X-Ray Computed Tomography Imaging. *J. Am. Chem. Soc.* **2007**, *129*, 7661−7665.
(27) Betzer, O.; Meir, R.; Motiei, M.; Yadid, G.; Popovtzer, R. Gold Nanoparticle-Cell Labeling Methodology for Tracking Stem Cells within the Brain. *Proc. SPIE* **2017**, *10077*, 100771F.
(28) Meir, R.; Motiei, M.; Popovtzer, R. Gold Nanoparticles for in Vivo Cell Tracking. *Nanomedicine (London, U. K.)* **2014**, *9*, 2059−2069.
(29) Meir, R.; Shamalov, K.; Betzer, O.; Motiei, M.; Horovitz-Fried, M.; Yehuda, R.; Popovtzer, A.; Popovtzer, R.; Cohen, C. J. Nanomedicine for Cancer Immunotherapy: Tracking Cancer-Specific T-Cells in Vivo with Gold Nanoparticles and CT Imaging. *ACS Nano* **2015**, *9*, 6363−6372.
(30) Meir, R.; Betzer, O.; Motiei, M.; Kronfeld, N.; Brodie, C.; Popovtzer, R. Design Principles for Noninvasive, Longitudinal and Quantitative Cell Tracking with Nanoparticle-Based CT Imaging. *Nanomedicine* **2017**, *13*, 421−429.
(31) Meir, R.; Popovtzer, R. Cell Tracking Using Gold Nanoparticles and Computed Tomography Imaging. *Wiley Interdiscip. Rev.: Nanomed. Nanobiotechnol.* **2017**, e1480.
(32) Matsumura, Y.; Maeda, H. A New Concept for Macromolecular Therapeutics in Cancer Chemotherapy: Mechanism of Tumoritropic Accumulation of Proteins and the Antitumor Agent Smancs. *Cancer Res.* **1986**, *46*, 6387−6392.
(33) Gerlowski, L. E.; Jain, R. K. Microvascular Permeability of Normal and Neoplastic Tissues. *Microvasc. Res.* **1986**, *31*, 288−305.
(34) Maeda, H. Toward a Full Understanding of the EPR Effect in Primary and Metastatic Tumors as Well as Issues Related to Its Heterogeneity. *Adv. Drug Delivery Rev.* **2015**, *91*, 3−6.
(35) Choi, K. Y.; Liu, G.; Lee, S.; Chen, X. Theranostic Nanoplatforms for Simultaneous Cancer Imaging and Therapy: Current Approaches and Future Perspectives. *Nanoscale* **2012**, *4*, 330−342.
(36) Cheng, Z.; Al Zaki, A.; Hui, J. Z.; Muzykantov, V. R.; Tsourkas, A. Multifunctional Nanoparticles: Cost *Versus* Benefit of Adding Targeting and Imaging Capabilities. *Science* **2012**, *338*, 903−910.
(37) Chen, H.; Zhang, W.; Zhu, G.; Xie, J.; Chen, X. Rethinking Cancer Nanotheranostics. *Nat. Rev. Mater.* **2017**, *2*, 17024.
(38) Enustun, B. V.; Turkevich, J. Coagulation of Colloidal Gold. *J. Am. Chem. Soc.* **1963**, *85*, 3317−3328.
(39) Moghimi, S. M.; Hunter, A. C.; Murray, J. C. Long-Circulating and Target-Specific Nanoparticles: Theory to Practice. *Pharmacol. Rev.* **2001**, *53*, 283−318.
(40) Abuchowski, A.; van Es, T.; Palczuk, N. C. Alteration of Immunological Properties of Bovine Serum Albumin by Covalent Attachment of Polyethylene Glycol. *J. Biol. Chem.* **1977**, *252*, 3578−3581.
(41) Qian, X.; Peng, X.-H.; Ansari, D. O.; Yin-Goen, Q.; Chen, G. Z.; Shin, D. M.; Yang, L.; Young, A. N.; Wang, M. D.; Nie, S. In Vivo Tumor Targeting and Spectroscopic Detection with Surface-Enhanced Raman Nanoparticle Tags. *Nat. Biotechnol.* **2007**, *26*, 83−90.
(42) Fixler, D.; Nayhoz, T.; Ray, K. Diffusion Reflection and Fluorescence Lifetime Imaging Microscopy Study of Fluorophore-Conjugated Gold Nanoparticles or Nanorods in Solid Phantoms. *ACS Photonics* **2014**, *1*, 900−905.
(43) Turgeman, L.; Fixler, D. Photon Efficiency Optimization in Time-Correlated Single Photon Counting Technique for Fluorescence Lifetime Imaging Systems. *IEEE Trans. Biomed. Eng.* **2013**, *60*, 1571−1579.
(44) Fixler, D.; Namer, Y.; Yishay, Y.; Deutsch, M. Influence of Fluorescence Anisotropy on Fluorescence Intensity and Lifetime Measurement: Theory, Simulations and Experiments. *IEEE Trans. Biomed. Eng.* **2006**, *53*, 1141−1152.
(45) Fixler, D.; Garcia, J.; Zalevsky, Z.; Weiss, A.; Deutsch, M. Speckle Random Coding for 2D Super Resolving Fluorescent Microscopic Imaging. *Micron* **2007**, *38*, 121−128.
(46) Fixler, D.; Tirosh, R.; Zinman, T.; Shainberg, A.; Deutsch, M. Differential Aspects in Ratio Measurements of [Ca2+]i Relaxation in Cardiomyocyte Contraction Following Various Drug Treatments. *Cell Calcium* **2002**, *31*, 279−287.

DOI: 10.1021/acsnano.7b05299
ACS Nano 2017, 11, 11127−11134